Excitation of Magnetosonic Waves in the Terrestrial Magnetosphere: Particle-in-cell Simulations

Kaijun Liu,[1] S. Peter Gary,[1] and Dan Winske[1]

Kaijun Liu, Los Alamos National Laboratory, Los Alamos, NM 87545, USA.(kaijun@lanl.gov)

S. Peter Gary, Los Alamos National Laboratory, Los Alamos, NM 87545, USA.(pgary@lanl.gov)

Dan Winske, Los Alamos National Laboratory, Los Alamos, NM 87545, USA.(winske@lanl.gov)

[1]Los Alamos National Laboratory, Los Alamos, New Mexico, USA.

Two-dimensional electromagnetic particle-in-cell simulations are performed to study the temporal development of an ion Bernstein instability driven by a proton velocity distribution with positive slope in the perpendicular velocity distribution function $f_p(v_\perp)$, where $\perp$ denotes directions perpendicular to the background magnetic field $\mathbf{B}_0$. The instability grows at propagation angles nearly perpendicular to $\mathbf{B}_0$, and at frequencies close to the harmonics of the proton cyclotron frequency. The simulated field fluctuation spectrum shows peaks near the first few harmonics of the proton cyclotron frequency and resembles observations of ULF waves, commonly referred to as fast magnetosonic waves, near the geomagnetic equator in the terrestrial magnetosphere. This growing mode may play an important role in the transverse heating of thermal protons and the acceleration of radiation-belt electrons.

1. Introduction

Enhanced field fluctuation spectra with peaks at frequencies close to the proton cyclotron frequency and its harmonics up to the lower hybrid resonance frequency have been observed near the geomagnetic equator of the terrestrial magnetosphere at radial distances between 2 and 8 R_E [*Russell et al.*, 1970; *Perraut et al.*, 1982; *Santolík et al.*, 2002]. The typical amplitude of the associated magnetic fluctuations is 0.03 $\sim$ 0.2 nT [*Perraut et al.*, 1982], which suggests $\delta B/B_0 \sim 10^{-4}$ ($\mathbf{B}_0$ is the background geomagnetic field). The waves propagate nearly perpendicular to $\mathbf{B}_0$, are primarily confined within 2 $\sim 3^\circ$ of the geomagnetic equator, and are mainly observed in the afternoon and premidnight sectors. Observations [*Perraut et al.*, 1982; *Boardsen et al.*, 1992; *Meredith et al.*, 2008] and theoretical studies [*Gul'elmi et al.*, 1975; *McClements et al.*, 1994; *Chen et al.*, 2010] suggest that the waves are driven by energetic protons at energies of tens keV which have ring-like distributions with $\partial f_p(v_\perp)/\partial v_\perp > 0$ ($f_p(v_\perp)$ is the perpendicular velocity distribution function).

These waves were first referred to as "equatorial noise" [*Russell et al.*, 1970], but more recently have been called "fast magnetosonic waves" because observations show that the wave magnetic field component is polarized along the background geomagnetic field [*Perraut et al.*, 1982] and the ratio of the electric field intensity to that of the magnetic field intensity is in good agreement with the theoretical values for fast magnetosonic waves at wave normal angles near 90° [*Boardsen et al.*, 1992]. These enhanced fluctuations are believed to play an important role in the transverse heating of thermal protons [*Horne*

et al., 2000] and the acceleration of radiation-belt electrons [*Horne and Thorne*, 1998; *Horne et al.*, 2007; *Shprits*, 2009; *Bortnik and Thorne*, 2010].

Denton et al. [2010] provide further insight into these enhanced fluctuations. Using both Cluster observations in the plasma sheet boundary layer and linear kinetic dispersion theory, they demonstrated that the waves are excited by a ring-type property of the proton velocity distribution. They also found that the wave properties change significantly with the proton beta (β_p). At $\beta_p \ll 1$, these fluctuations are predominantly electrostatic, suggesting that these waves are more accurately described as ion Bernstein waves [*Janhunen et al.*, 2003; *Ashour-Abdalla et al.*, 2006]. As β_p approaches unity, the waves develop a strong electromagnetic component. The excited magnetic field fluctuations have components in both the perpendicular and parallel directions (with regard to $\mathbf{B}_0$), but the perpendicular fluctuations are larger. More interestingly, the parallel magnetic fluctuations $\delta B_{\parallel}$ become dominant when β_p is further increased, which resembles the fluctuations referred to as fast magnetosonic waves that are observed near the geomagnetic equator in the terrestrial magnetosphere. These results have been confirmed by *Gary et al.* [2010], who further pointed out that the maximum instability growth rate decreases with increasing electron-to-proton temperature ratio.

Although some simulation studies have addressed the ion Bernstein instability in the electrostatic limit [*Lee and Birdsall*, 1979; *Janhunen et al.*, 2003], no simulations have addressed the fully electromagnetic properties of this instability in the high β_p regime appropriate for the magnetosphere. The present study carries out two-dimensional (two spatial dimensions, but all three velocity components retained) electromagnetic particle-

in-cell (PIC) simulations to investigate the properties of the ion Bernstein instability driven by proton distributions with $\partial f_p(v_\perp)/\partial v_\perp > 0$ and $\beta_p \sim 1$. The PIC code used is a reduced version of the three-dimensional PIC model in *Liu et al.* [2006] and has been successfully applied to the study of particle energization by oblique inertial Alfvén waves in the auroral region [*Seyler and Liu*, 2007]. The simulation results demonstrate that the ion Bernstein instability grows at propagation angles nearly perpendicular to $\mathbf{B}_0$, with a fluctuating field spectrum with peaks at frequencies close to the first few harmonics of the proton cyclotron frequency, in agreement with recent theory [*Denton et al.*, 2010; *Gary et al.*, 2010] and observations of fast magnetosonic waves.

2. Simulation Results

The two-dimensional simulation domain lies in the $x - y$ plane and the background magnetic field is in the y direction. Periodic boundary conditions are used in both dimensions. Due to the nearly perpendicular propagation of the instability, we choose $L_x = 9.6\lambda_i$, $N_x = 128$, $L_y = 64\lambda_i$, and $N_y = 64$, where $\lambda_i = \sqrt{m_p/n_0\mu_0 e^2}$ is the ion inertial length. Other relevant parameters are $m_p/m_e = 100$, $\omega_p/\Omega_p = 15$ ($\omega_p = \sqrt{n_0 e^2/\epsilon_0 m_p}$ is the proton plasma frequency and $\Omega_p = eB_0/m_p$ is the proton cyclotron frequency), and the time step length is $\delta t\Omega_p = 0.001$. The present simulation has 2000 ions and 2000 electrons in each cell. The reduced proton-to-electron mass ratio and the relatively small ω_p/Ω_p used here are to enable a large time step. Although they slightly affect the properties of the ion Bernstein instability, they do not change the essential physics, as will be discussed in section 3.

Following *Denton et al.* [2010] and *Gary et al.* [2010], a subtracted Maxwellian distribution is used to initialize the protons in the simulation,

$$f_p(\mathbf{v}) = f_1(\mathbf{v}) - f_2(\mathbf{v}), \tag{1}$$

with

$$f_j(\mathbf{v}) = \frac{n_j}{(\pi v_j^2)^{3/2}} \exp(-v^2/v_j^2). \tag{2}$$

Here $v^2 = v_\parallel^2 + v_\perp^2$, $v_j = \sqrt{2T_j/m_j}$ is the jth species thermal speed (both are protons). This distribution is still isotropic although non-Maxwellian. This simplifies the physics involved by excluding the possible development of the Alfvén cyclotron instability which can be driven by anisotropic protons [*Gary*, 1993]. We choose the dimensionless parameters to be $n_1/n_0 = 6.3$, $n_2/n_0 = 5.3$, $T_1/(m_p v_A^2) = 0.4$, T_2/T_1=0.9, where n_0 is the background plasma density and v_A is the Alfvén velocity. Note that $n_2/n_1 < (T_2/T_1)^{3/2}$ is required to avoid negative values in $f_p(\mathbf{v})$. With these parameters, $\beta_p = (n_1T_1 - n_2T_2)/(B_0^2/2\mu_0) = 2(n_1T_1 - n_2T_2)/(n_0 m_p v_A^2) = 1.2$ and the black line in Figure 1 illustrates the reduced perpendicular velocity distribution

$$\begin{aligned} f_p(v_\perp) &= \int_{-\infty}^{\infty} dv_\parallel \int_0^{2\pi} d\phi f_p(\mathbf{v}) \\ &= \frac{2n_1}{v_1^2} \exp(-v^2/v_1^2) - \frac{2n_2}{v_2^2} \exp(-v^2/v_2^2), \end{aligned} \tag{3}$$

where ϕ is the azimuthal angle of the perpendicular velocity component. The reduced perpendicular velocity distribution has positive $\partial f_p(v_\perp)/\partial v_\perp$ in the range of $0 < v_\perp < 0.5 v_A$. Electrons in the simulation have a Maxwellian distribution and $T_e/T_1 = 0.01$.

Linear kinetic dispersion theory for electromagnetic fluctuations in a homogeneous, magnetized, collisionless plasma is first applied to the instability analysis. The Cartesian

coordinate system of the linear dispersion analysis [*Gary*, 1993] admits spatial variations in both the direction parallel to $\mathbf{B}_0$ (denoted by $\|$) and one direction perpendicular to the background field (denoted by $\perp$), but no spatial variations in the other perpendicular direction (denoted by $\perp\perp$). The $\perp$, $\|$, and $\perp\perp$ directions correspond to the x, y, and z directions in the simulations, respectively. So the wavevector is defined as $\mathbf{k} = k_\perp \hat{\mathbf{x}} + k_\| \hat{\mathbf{y}}$ and the complex frequency is $\omega = \omega_r + i\gamma$ where $\gamma > 0$ represents temporal growth of a fluctuating normal mode of the plasma.

For the initial proton distribution shown in Figure 1 and the plasma parameters stated above, the ion Bernstein instability is found to grow at frequencies near the first two proton cyclotron harmonics ($\omega \approx \Omega_p$, $2\Omega_p$). The growth rates as a function of $k_\perp \lambda_i$ and propagation angle θ (with regard to $\mathbf{B}_0$) for waves near the first and the second proton cyclotron harmonics are displayed in the left panel and the right panel of Figure 2, respectively. The asterisk in each panel represents the location of the local maximum growth rate γ_{max}. For waves of $\omega \approx \Omega_p$, $\gamma_{max}/\Omega_p = 0.044$ at $k_\perp \lambda_i \approx 4.8$ and $\theta \approx 85.8°$. For waves of $\omega \approx 2\Omega_p$, $\gamma_{max}/\Omega_p = 0.034$ at $k_\perp \lambda_i \approx 9.3$ and $\theta \approx 86.8°$. The solid black contour line in each panel represents the contour of $\gamma/\Omega_p = 0.03$. The instability can grow over wide ranges of $k_\perp \lambda_i$ and θ with significant growth rates. Linear analysis also shows that the amplitude relations among electric and magnetic field components of these waves are $\delta E_\perp \gg \delta E_{\perp\perp} \gg \delta E_\|$ and $\delta B_{\perp\perp} \geq \delta B_\| \gg \delta B_\perp$, but the amplitude relation between $\delta B_{\perp\perp}$ and $\delta B_\|$ changes with β_p quite significantly. The compressible component $\delta B_\|$ starts to dominate as β_p increases.

Figure 3 displays the time evolution of the energies in different electric and magnetic field components in the simulation. The instability is weak and saturates at a very low level so that an exponential growth phase of the energies does not clearly stand out in Figure 3. The thermal noise level is still relatively high, although the simulation has 2000 particles per cell, which is limited by the computational resources available. Nevertheless, the saturation levels shown by Figure 3 are reliable and physical, because another simulation with 1000 particles per cell gave the same saturation levels. Figure 3 further shows that $\delta E_\perp \gg \delta E_{\perp\perp} \gg \delta E_\parallel$ and $\delta B_{\perp\perp} \geq \delta B_\parallel \gg \delta B_\perp$, in agreement with the linear kinetic analysis results. Note that the dominant electric field component is $\delta E_\perp$, which is mainly the electrostatic contribution, given the nearly perpendicular propagation of the instability.

Figure 4 displays the compressive magnetic fluctuations from the simulation at $t\Omega_p = 60$. The top panel shows the contour plot of B_y/B_0, while the bottom panel presents the spatial power spectrum of $\delta B_y = B_y - B_0$. The two solid black contour lines in the bottom panel are the same ones in Figure 2 but are now plotted in the $k_\perp\lambda_i$-$k_\parallel\lambda_i$ coordinates. They represent the contours of $\gamma/\Omega_p = 0.03$ given by linear kinetic dispersion theory for waves near the first two proton cyclotron harmonics. The lower left contour is for the first harmonic while the upper right contour is for the second harmonic. The regions of enhanced fluctuations are close to the two contours and reveal the growth of the waves near the first two proton cyclotron harmonics. This is further confirmed by Figure 5, which presents the temporal spectrum of δB_y at $x = 4.8\lambda_i$ and $y = 32\lambda_i$ from $t\Omega_p = 50$ to $t\Omega_p = 100$. Spectral peaks at $\omega \approx \Omega_p$, $2\Omega_p$ are clear, in agreement with the prediction

of linear kinetic theory that the instability is unstable near the first two proton cyclotron harmonics.

Compared with the $\gamma/\Omega_p = 0.03$ contours, the regions of enhanced fluctuations seem to shift toward small $k_\perp \lambda_i$ slightly. This shift might be due to the nonlinear evolution of the simulation system. Linear kinetic analysis suggests that the properties of the instability are very sensitive to the proton distribution. The proton distribution evolves with time in the simulation due to wave-particle interactions, as shown in Figure 1. The dashed red line, the green line, and the blue line represent $f_p(v_\perp)$ derived from the simulation at $t\Omega_p = 0$, 60, and 100, respectively. The positive slope in $f_p(v_\perp)$ is gradually reduced by the development of the instability.

3. Summary and Discussion

The general properties of an ion Bernstein instability driven by a proton velocity distribution with positive slope in $f_p(v_\perp)$ at $\beta_p \sim 1$ are studied using linear kinetic dispersion theory and two-dimensional electromagnetic PIC simulations. The present results demonstrate that the instability grows at propagation angles nearly perpendicular to $\mathbf{B}_0$, saturates at a very low level, and yields spectral peaks at frequencies close to the first few harmonics of the proton cyclotron frequency. These features resemble the observed fast magnetosonic waves near the geomagnetic equator in the terrestrial magnetosphere.

Linear kinetic dispersion analysis for the same initial proton distribution using realistic proton-to-electron mass ratio ($m_p/m_e = 1836$) and $\omega_p/\Omega_p = 294$ has been reported by *Gary et al.* [2010]. They found that the ion Bernstein instability grows at frequencies near the proton cyclotron harmonics up to $\omega \approx 5\Omega_p$. The maximum growth rate decreases as

the harmonic number increases. For waves of $\omega \approx \Omega_p$, $\gamma_{max}/\Omega_p = 0.038$ at $k_\perp \lambda_i \approx 4.87$ and $\theta \approx 86.7°$. For waves of $\omega \approx 2\Omega_p$, $\gamma_{max}/\Omega_p = 0.036$ at $k_\perp \lambda_i \approx 8.73$ and $\theta \approx 87.9°$. The comparison of the linear kinetic analysis results discussed in section 2 with the work of *Gary et al.* [2010] shows that the reduced proton-to-electron mass ratio and the relatively small ω_p/Ω_p used in the present study slightly affect the properties of the ion Bernstein instability, but do not change the essential physics.

A simple subtracted Maxwellian distribution is used to construct the positive slope in $f_p(v_\perp)$ in the present study because our linear kinetic dispersion code is based on bi-Maxwellian velocity distributions [*Gary*, 1993]. Since $n_2/n_1 < (T_2/T_1)^{3/2}$ is required in equation (1) to avoid negative values of $f_p(\mathbf{v})$, only moderately positive slopes in $f_p(v_\perp)$ can be used. While our results show that the maximum growth rate is near the fundamental proton cyclotron harmonic for the given proton distribution, some observations [*Boardsen et al.*, 1992] show spectra which peak at higher harmonics of the proton cyclotron frequency and linear theories based upon more strongly unstable distributions similarly predict maximum growth at higher harmonics [*Gul'elmi et al.*, 1975; *Horne et al.*, 2000]. We find that the growth rates of the ion Bernstein instability near different proton cyclotron harmonics are very sensitive to the proton distributions which drive it. More linear kinetic analysis and PIC simulations are needed to further understand the relationship between the ion free energy and the maximum growing modes.

In order to study the effect of the excited electromagnetic fluctuations on the thermal protons, another PIC simulation similar to the one discussed in section 2 but with an additional component representing thermal protons has been performed. This run shows

that the ion Bernstein instability extracts energy from the energetic protons and transfers the energy into the transverse kinetic energy of the thermal protons and the parallel kinetic energy of the background electrons. These results will be described in more detail elsewhere.

Acknowledgments. This work was performed under the auspices of the U.S. Department of Energy (DOE). It was supported primarily by the Defense Threat Reduction Agency under the "Basic Research for Combating Weapons of Mass Destruction (WMD)" Program, project IACRO # 07-4323I, with additional support from the Heliospheric Guest Investigators Program of the National Aeronautics and Space Administration.

References

Ashour-Abdalla, M., J. N. Leboeuf, D. Schriver, J.-M. Bosqued, N. Cornilleau-Wehrlin, V. Sotnikov, A. Marchaudon, and A. N. Fazakerley (2006), Instabilities driven by ion shell distributions observed by Cluster in the midaltitude plasma sheet boundary layer, *J. Geophys. Res.*, *111*, A10223, doi:10.1029/2005JA011490.

Boardsen, S., D. Gallagher, D. Gurnett, W. Peterson, and J. Green (1992), Funnel-shaped, low-frequency equatorial waves, *J. Geophys. Res.*, *97*(A10), 14,967.

Bortnik, J., and R. M. Thorne (2010), Transit-time scattering of energetic electrons due to equatorially-confined magnetosonic waves, *J. Geophys. Res.*, *115*, A07213, doi: 10.1029/2010JA015283.

Chen, L., R. M. Thorne, V. K. Jordanova, and R. B. Horne (2010), Global simulation of magnetosonic waves instability in the storm time magnetosphere, *J. Geophys. Res.*,

submitted.

Denton, R. E., M. J. Engebretson, A. Keiling, A. P. Walsh, S. P. Gary, P. M. E. Décréau, C. A. Cattell, K.-H. Glassmeier, and H. Rème (2010), Multiple harmonic ULF waves in the plasma sheet boundary layer: Instability analysis, *J. Geophys. Res.*, submitted.

Gary, S. P. (1993), *Theory of space plasma microinstabilities*, Cambridge Univ. Press, New York.

Gary, S. P., K. Liu, D. Winske, and R. E. Denton (2010), Ion Bernstein instability in the terrestrial magnetosphere: Linear dispersion theory, *J. Geophys. Res.*, submitted.

Gul'elmi, A. V., B. I. Klaine, and A. S. Potapov (1975), Excitation of magnetosonic waves with discrete spectrum in the equatorial vicinity of the plasmapause, *Planet. Space Sci.*, *23*, 279.

Horne, R., G. Wheeler, and H. Alleyne (2000), Proton and electron heating by radially propagating fast magnetosonic waves, *J Geophys Res*, *105*, A12.

Horne, R. B., and R. M. Thorne (1998), Potential waves for relativistic electron scattering and stochastic acceleration during magnetic storms, *Geophys. Res. Lett.*, *25*(15), 3011.

Horne, R. B., R. M. Thorne, S. A. Glauert, N. P. Meredith, D. Pokhotelov, and O. Santolík (2007), Electron acceleration in the van allen radiation belts by fast magnetosonic waves, *Geophys. Res. Lett.*, *34*, L17107, doi:10.1029/2007GL030267.

Janhunen, P., A. Olsson, A. Vaivads, and W. K. Peterson (2003), Generation of Bernstein waves by ion shell distributions in the auroral region, *Ann. Geophys.*, *21*(4), 881.

Lee, J. K., and C. K. Birdsall (1979), Velocity space ring-plasma instability, magnetized, part ii: Simulation, *Phys. Fluids*, *22*(7), 1315.

Liu, K., C. E. Seyler, and T. Xu (2006), Particle-in-cell simulations of current shear-driven instabilities and the generation of broadband ELF fluctuations, *J Geophys Res*, *111*, A11307, doi:10.1029/2006JA011858.

McClements, K., R. Dendy, and C. Lashmore-Davies (1994), A model for the generation of obliquely propagating ULF waves near the magnetic equator, *J. Geophys. Res.*, *99*(A12), 23,685.

Meredith, N. P., R. B. Horne, and R. R. Anderson (2008), Survey of magnetosonic waves and proton ring distributions in the Earth's inner magnetosphere, *J Geophys Res*, *113*, A06213, doi:10.1029/2007JA012975.

Perraut, S., A. Roux, P. Robert, R. Gendrin, J.-A. Sauvaud, J.-M. Bosqued, G. Kremser, and A. Korth (1982), A systematic study of ULF waves above F_{H^+} from GEOS 1 and 2 measurements and their relationships with proton ring distributions, *J. Geophys. Res.*, *87*(A8), 6219.

Russell, C., R. Holzer, and E. Smith (1970), OGO 3 observations of ELF noise in the magnetosphere, 2. the nature of the equatorial noise, *J. Geophys. Res.*, *75*(4), 755.

Santolík, O., J. S. Pickett, D. A. Gurnett, M. Maksimovic, and N. Cornilleau-Wehrlin (2002), Spatiotemporal variability and propagation of equatorial noise observed by cluster, *J. Geophys. Res.*, *107*(A12), 1495, doi:10.1029/2001JA009159.

Seyler, C. E., and K. Liu (2007), Particle energization by oblique inertial alfvén waves in the auroral region, *J. Geophys. Res.*, *112*, A09302, doi:10.1029/2007JA012412.

Shprits, Y. Y. (2009), Potential waves for pitch-angle scattering of near-equatorially mirroring energetic electrons due to the violation of the second adiabatic invariant, *Geophys.*

Res. Lett., *36*, L12106, doi:10.1029/2009GL038322.

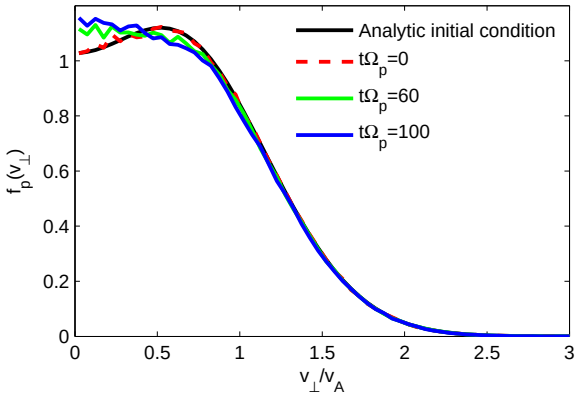

Figure 1. The perpendicular velocity distributions of the protons. The black line displays $f_p(v_\perp)$ of Equation (3), which is used in the linear kinetic dispersion analysis and as an initial condition in the PIC simulations. The dashed red line, the green line, and the blue line represent $f_p(v_\perp)$ derived from the present simulation at $t\Omega_p = 0$, 60, and 100, respectively.

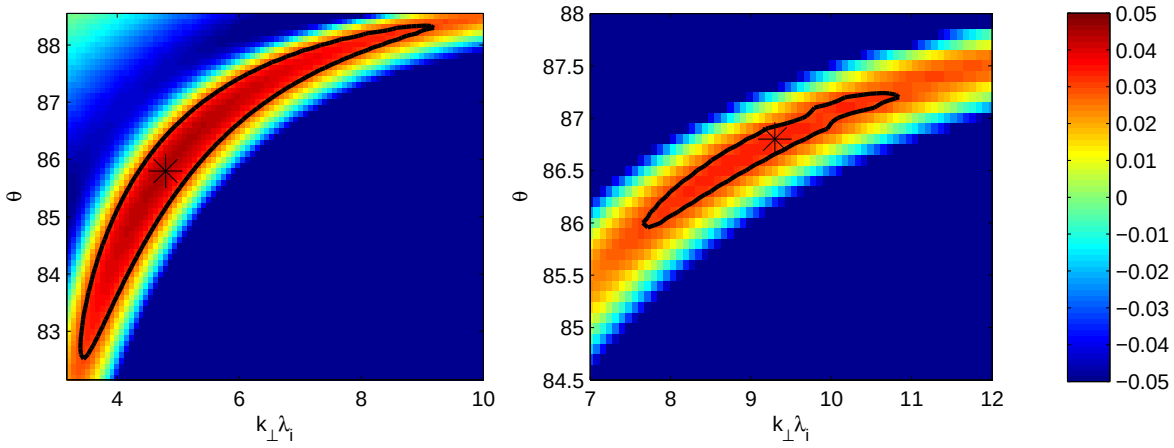

Figure 2. Linear dispersion theory results: Growth rates as a function of $k_\perp \lambda_i$ and propagation angle θ (with regard to $\mathbf{B}_0$) for waves near the first (left panel) and the second (right panel) proton cyclotron harmonics. The asterisk in each panel represents the location of the local maximum growth rate. The solid black contour line in each panel represents the contour of $\gamma/\Omega_p = 0.03$. Note that the minimum value of the color scale corresponds to $\gamma/\Omega_p = -0.05$ so larger damping rates saturate in the plot.

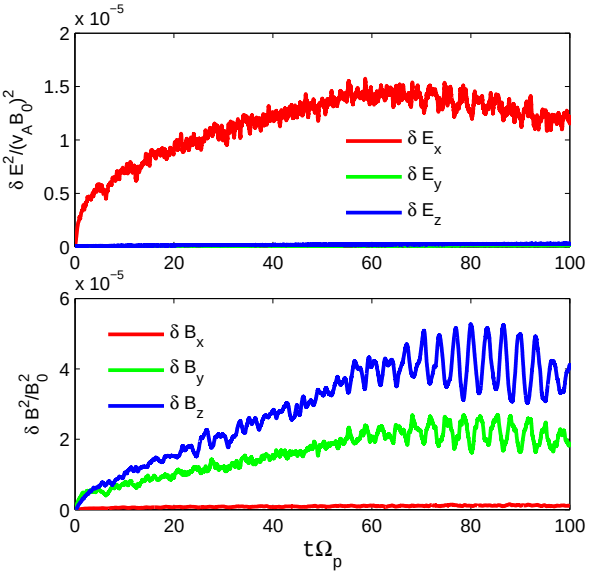

Figure 3. PIC simulation results: The time evolution of the energies in different electric (Top) and magnetic (Bottom) field components.

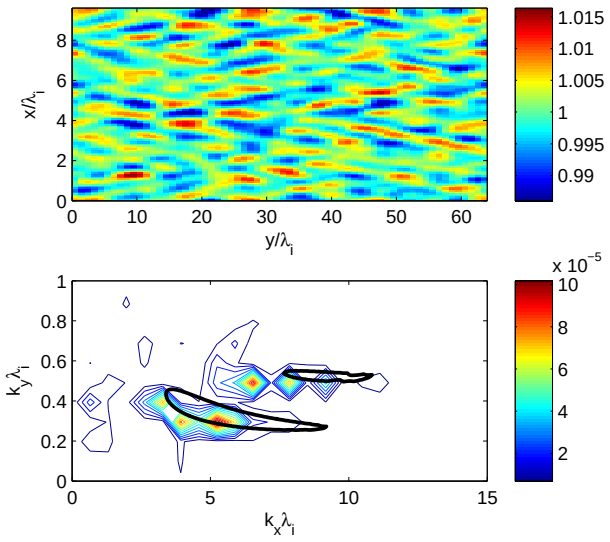

Figure 4. PIC simulation results: The compressive magnetic fluctuations at $t\Omega_p = 60$. Top panel: The contour plot of B_y/B_0. Bottom panel: The spatial power spectrum of $\delta B_y = B_y - B_0$. The two solid black contour lines in the bottom panel are the same ones in Figure 2 but are now plotted in the $k_\perp\lambda_i$-$k_\parallel\lambda_i$ coordinates. They represent the contours of $\gamma/\Omega_p = 0.03$ given by linear kinetic dispersion theory for waves near the first two proton cyclotron harmonics. The lower left contour is for the first harmonic while the upper right contour is for the second harmonic.

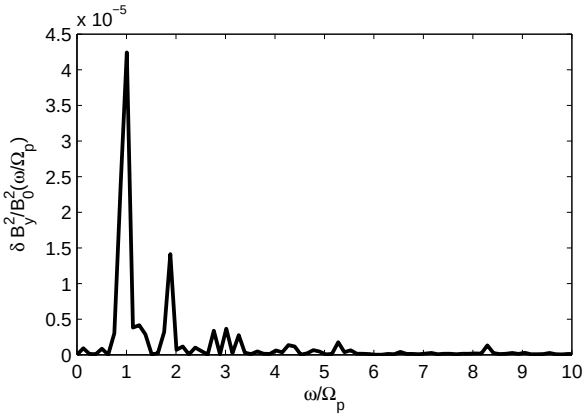

Figure 5. PIC simulation results: The temporal spectrum of δB_y at $x = 4.8\lambda_i$ and $y = 32\lambda_i$ from $t\Omega_p = 50$ to $t\Omega_p = 100$.